ELSEVIER

Ultramicroscopy 78 (1999) 125–139

ultramicroscopy

# Practical aspects of atomic resolution imaging and analysis in STEM

E.M. James*, N.D. Browning

*Department of Physics (M/C 273), University of Illinois at Chicago, 845 W. Taylor Street, Chicago, IL, 60607-7059, USA*

Received 29 October 1998; received in revised form 29 December 1998

**Abstract**

In the scanning transmission electron microscope (STEM), the spatial resolution of experimental images and spectra is determined by the size and stability of the electron probe. Atomic resolution, of 0.2 nm and under, is possible if all experimental parameters influencing probe formation are carefully optimized. Here, the formation and alignment of the STEM probe using electron Ronchigrams is described. Practical examples of probe formation, Z-contrast imaging and electron energy-loss spectroscopy (EELS) are demonstrated on a Schottky field emission, JEOL JEM-2010F microscope. Single crystal Si ⟨1 1 0⟩ images were used for resolution testing and showed that probe sizes of under 0.14 nm are obtainable. A 36.5° Σ5 tilt grain boundary in nominally iron doped $SrTiO_3$ was imaged incoherently and analyzed with EELS, using this probe. © 1999 Elsevier Science B.V. All rights reserved.

*Keywords:* STEM; Z-contrast imaging; EELS; Atomic resolution

## 1. Introduction

The ability to form a small, bright electron probe in the scanning transmission electron microscope (STEM) is important since this is what limits the spatial resolution of imaging and analytical techniques such as electron energy-loss spectroscopy (EELS). For probe intensity distribution widths of 0.2 nm and under, these techniques can yield atomic resolution information from crystalline specimens and their defects [1–3]. The majority of previous experimental results have been obtained from dedicated scanning microscopes using the cold field emission electron source. However, the principles of probe formation, and the crucial criteria to be optimized are the same for any modern transmission electron microscope. Here we show the procedure of aligning the probe, using an electron Ronchigram, on a JEOL JEM-2010F instrument. The Ronchigram, alternatively known as a shadow image, or microdiffraction pattern, contains a wealth of information on the specimen and also on the operating conditions of the instrument and its probe-forming optics [4]. After accurate alignment, the STEM resolution of the microscope is demonstrated to be 0.14 nm in scanned, Z-contrast (high-angle annular dark-field) images of atomic columns in single-crystal silicon. This is therefore approximately the size of the probe. An estimate of its intensity profile is then possible by investigating the strength at which certain periodicities in the silicon specimen are passed to the image.

* Corresponding author. Tel.: + 1-312-9965477; fax: + 1-312-9964451.

*E-mail address:* edjames@uic.edu (E.M. James)

0304-3991/99/$ - see front matter © 1999 Elsevier Science B.V. All rights reserved.
PII: S0304-3991(99)00018-2

Many crystalline specimens can be studied in the high-resolution STEM. As an example, a $\Sigma 5$ grain boundary in strontium titanate has been imaged with the small probe. Z-contrast images show the atomic column arrangement at the interface between the two perfect crystals. It is possible to stop scanning of the probe and acquire EELS spectra from regions of the grain boundary, without changing any microscope optical settings. This method provides an avenue of chemical and electronic structure analysis of materials on the scale of individual atom columns.

## 2. Experimental STEM operation

### 2.1. Formation of the probe

Fig. 1 shows the electron optical arrangement of the probe-forming system in the JEOL JEM-2010F. An electrostatic gun lens and twin condenser lens system controls de-magnification of the Schottky field emission source. The microscope is a standard model TEM with a free-lens control that is used to set suitable lens currents for small probe formation. Compared to the cold field emitter generally used in dedicated STEM, the Schottky electron source has a much larger emission area. Each element of the source is assumed to emit incoherently and therefore leads to an incoherent broadening of the probe [5]. However, a large de-magnification factor between source and probe reduces this probe-broadening effect. This is at the expense of decreasing the amount of current at low angles that is not intercepted by the probe-forming aperture. In particular, by using the C1 lens near maximum excitation, a cross-over is formed between the two condensers and a large source de-magnification can then be achieved. This is probably a factor of ten greater than is necessary in the cold field emission STEM [6]. C2 and the gun lens can then be used to tune the probe coherence further, depending on the probe size that is required. Once these lens settings have been preset, it

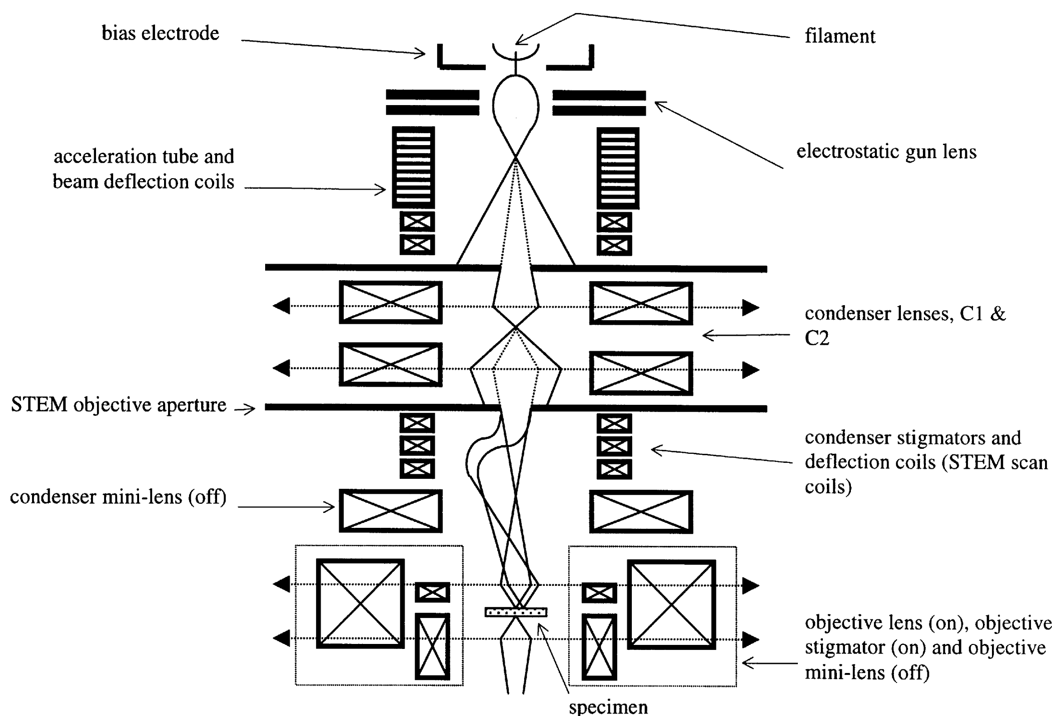


Fig. 1. Schematic diagram of the probe-forming electron optics in the JEOL JEM-2010F transmission electron microscope.

is trivial to switch between STEM and optimum conventional TEM (CTEM) operating conditions.

### 2.2. Probe alignment optimization

The electron "Ronchigram", or "shadow image" is one of the most useful ways of characterizing and optimizing the probe. This is because the intensity, formed at the microscope Fraunhofer diffraction plane, varies considerably with angle, and this variation is a very sensitive function of lens aberrations and defocus [4]. When the excitation of each illumination electron optical component is slightly changed, very small misalignments become apparent by translations in the pattern that depart from circular symmetry. Furthermore, the presence or absence of interference fringes in the pattern indicates the amount of incoherent probe broadening due to instabilities and the effect of a finite source size. Fig. 2 shows schematically the ray diagram for Ronchigram formation. The probe remains stationary and the post-specimen intensity is recorded as a function of angle by a CCD camera or equivalent device. Very high illumination convergence angles are allowed. Examples, where this alignment method has been used, include the impressive atomic resolution Z-contrast images from the 300 kV STEM [7,8], "super-resolution" aperture synthesis experiments [9], and analysis of the performance of STEM spherical aberration correctors [10].

Experimentally, to observe the Ronchigram, apertures are removed after the specimen and a large probe convergence angle ( > 100 mrad) is selected by inserting the largest STEM objective aperture: in the JEM-2010F, this corresponds to the CTEM condenser aperture. The Ronchigram can then be directly observed on the microscope phosphor screen. Camera length and positioning are controlled with the projector lenses and shift coils. Alternatively, the Ronchigram can be observed on a TV-rate CCD camera positioned beneath the phosphor screen.

Typical Ronchigrams at the amorphous edge of a specimen are shown in Fig. 3. At large defocus, the electron cross-over is at a relatively large distance from the specimen, along the optic axis, and a projection image is observed. As Gaussian focus

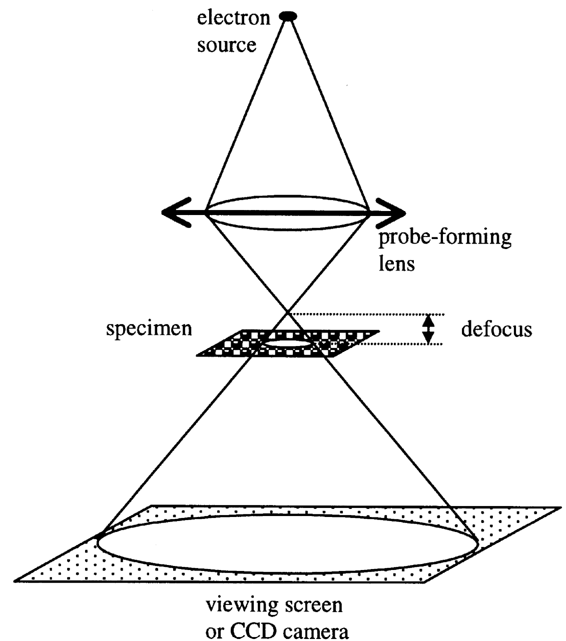


Fig. 2. A ray diagram showing formation of an electron Ronchigram. Only one probe-forming lens is shown: experimentally, this is the objective lens pre-field. For simplicity, beam compression caused by the objective lens post-field, and the effects of any post specimen lenses are not shown.

is approached, an angular dependence to the magnification emerges, due to lens aberrations and the manner in which they change the phase of the electron beam. At slight underfocus, the azimuthal and radial circles of infinite magnification can be seen [4]. These are the angles at which defocus and spherical aberration effectively cancel and are characteristic of Ronchigrams from a round, probe-forming lens. Axial astigmatism can be very accurately corrected by exciting the stigmator coils so that these Ronchigram features are circularly symmetric. As the beam is focused, the central, low angles display the highest magnification. The coma free axis is clearly defined by this position and all alignment and positioning of detectors and apertures can be performed with respect to this spot. The prime advantage of using a Ronchigram is that the coma-free axis is directly visible. In other alignment methods, the current or voltage center of the objective lens must be used as the reference and this is not always sufficiently accurate. Next, the

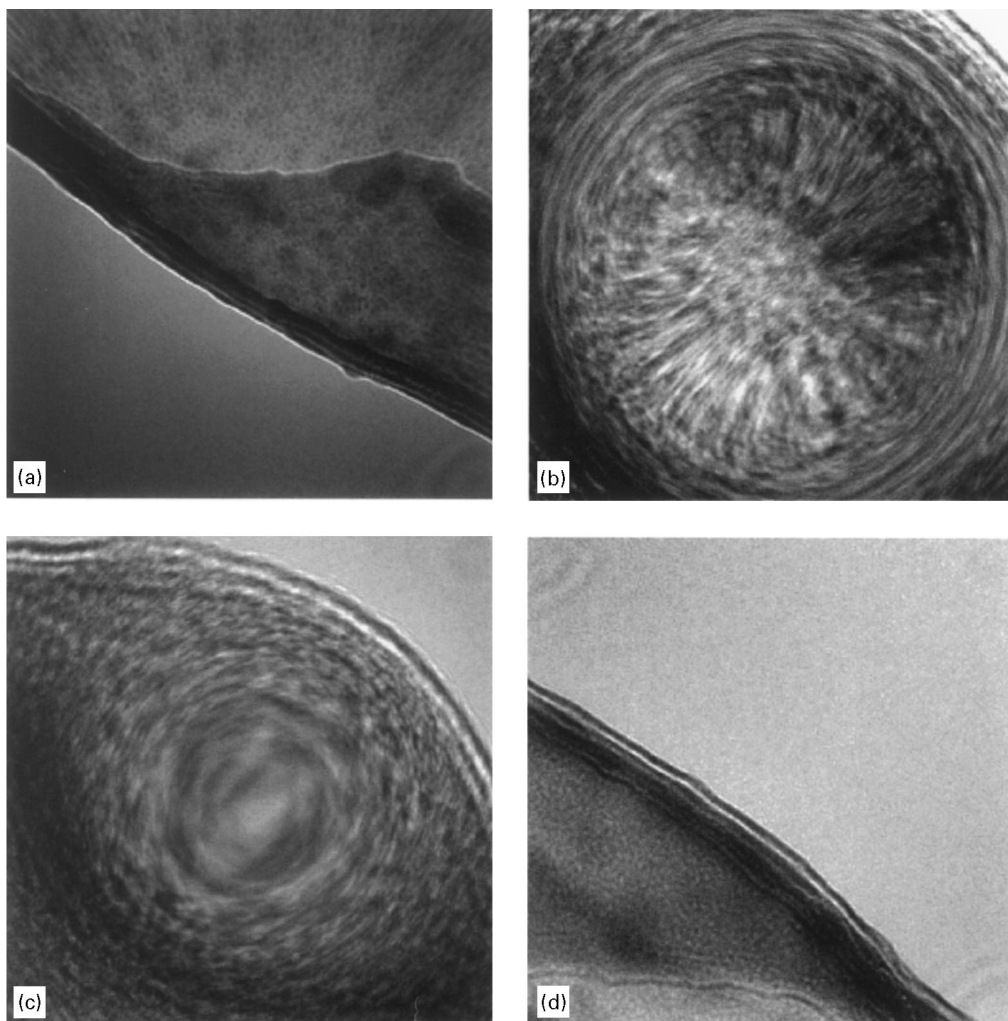


Fig. 3. Experimental electron Ronchigrams of a thin amorphous carbon layer. (a) large underfocus – rays at all angles cross the optic axis after the specimen and a shadow image of the specimen edge is seen. (b) small underfocus – low angle rays cross the optic axis after the specimen. High-angle rays cross before the specimen, because of the effect of spherical aberration. The shadow image therefore changes in magnification as a function of angle and critical angles occur where there is infinite radial and azimuthal magnification. Departures from circular symmetry indicate the presence of astigmatism. (c) Gaussian focus – the lowest angle rays cross the axis at the specimen; higher angle rays cross before it, due to the effect of spherical aberration. (d) overfocus – rays at all angles cross the axis before the specimen and a shadow image of the specimen edge is visible.

illumination beam alignment can be very accurately checked by wobbling first the condenser lens excitation and then the microscope high tension. If there is a misalignment of the beam between condenser and objective lenses, there will be a periodic translation of Ronchigram features as the wobbling takes place. This can be corrected using the condenser alignment coils (CTEM bright tilt) so that the features only oscillate in and out symmetrically about the coma-free axis. For the JEM-2010F, a change in the extraction voltage and gun lens potential by small amounts has little effect on the Ronchigram. This is possibly due to the high de-magnification of the source. Any instabilities in

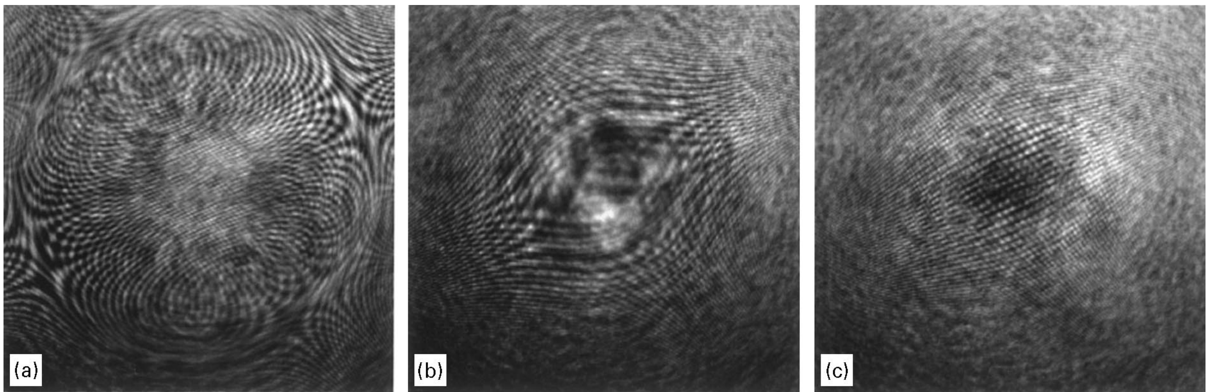


Fig. 4. Ronchigrams of a thin region of silicon ⟨1 1 0⟩ showing diffraction effects and fringes arising from the specimen periodicities. Visibility of the characteristic fringes depends on precise tilting of the specimen and the amount of probe coherence in a direction perpendicular to the relevant crystal lattice plane. (a) small underfocus – lattice fringes are visible near the Ronchigram center and they become heavily distorted further out in angle. The distortion is due to phase changes introduced by the lens spherical aberration. (b) near Scherzer focus – the central fringes become large and wide. Their area corresponds to the entire overlap region between zero-order and relevant diffracted beams. (c) slight overfocus – fringes are visible with size and spacing that decreases with increasing angle from the Ronchigram center.

these voltages are therefore thought to be insignificant in determining the probe size.

The probe has now been aligned with respect to the coma-free axis. Control of its intensity distribution is now dependent on the exact illumination lens settings and the size of the STEM objective aperture that is subsequently inserted to exclude aberrated beams at high angles. Fig. 4 shows Ronchigrams from a thin region of Si ⟨1 1 0⟩ at slight defoci. Diffraction effects are clearly present in the pattern and lattice fringes are observed if the probe coherence is great enough. It is the movement of these fringes across the relevant STEM detectors, as the probe is scanned, that gives rise to image contrast. At high angles in the Ronchigram, the fringes are distorted because of spherical aberration of the objective lens pre-field. This effect is lucid in Fig. 5, a Ronchigram of silicon ⟨1 1 1⟩. Fringes correspond to the 0.192 nm {2 2 0} planar spacing. Their distortion, a function of angle from the center, is circularly symmetric, as expected when spherical aberration is the only aberration of significance. At low angles the hexagonal arrangement of the lattice planes is more obvious from the fringe pattern. Analysis of such Ronchigrams, and derivation of electron optical parameters from them, has been carried out by Lin and Cowley [11]. Also, at large defocus, when a shadow image at low magnification is visible, the crystal Kikuchi lines are seen (Fig. 6). Since the coma-free axis position is already known, it is simple to adjust the specimen tilt so that the desired zone axis is aligned precisely, for the sub-micron specimen area that is of interest.

### 2.3. Z-contrast imaging

Once the probe has been successfully aligned and stigmated, the probe intensity distribution full-width at half-maximum (FWHM) depends most critically on the focus setting; the illumination convergence angle (set by an aperture); the spherical aberration of the objective lens; and the level of any incoherent broadening of the probe by instabilities and the effect of a finite source size. In general, the Scherzer focus condition [12] approximately minimizes this quantity. Z-contrast images can be formed by detecting intensity on a large post-specimen annular detector as the probe is rastered. If the detector inner-angle is large enough (the order of 100 mrad), the image resolution is given by the probe intensity distribution width, to a high degree of accuracy [13,14]. Such images are typically much more readily interpretable than conventional HRTEM micrographs, without complicated

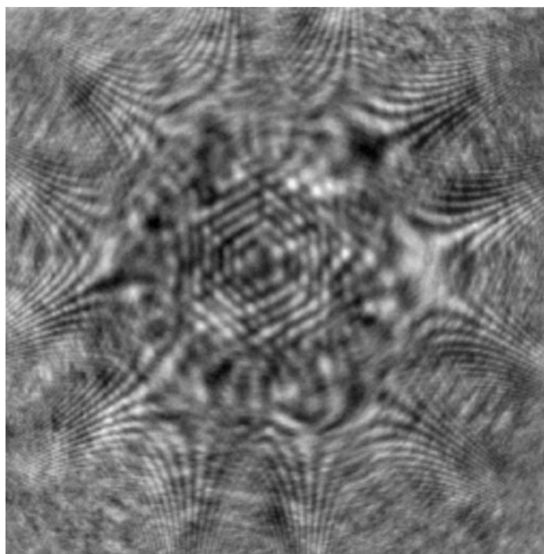

Fig. 5. Ronchigram of a thin region of silicon ⟨1 1 1⟩. Interference gives rise to fringes corresponding to the 0.192 nm {2 2 0} periodicity. Spherical aberration of the probe-forming optics causes significant distortions of the hexagonal pattern away from the center.

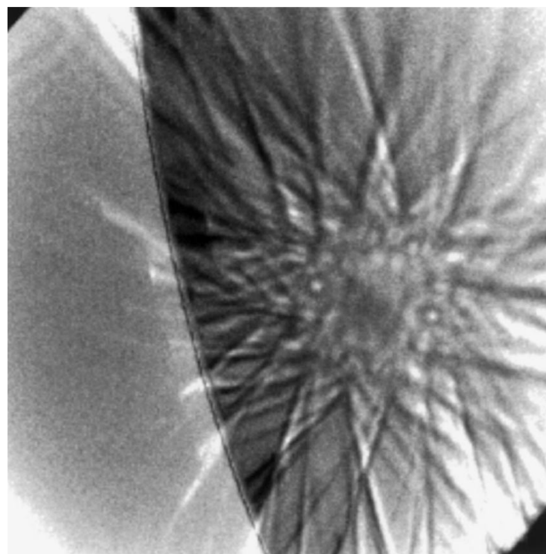

Fig. 6. Ronchigram at the edge of a silicon ⟨1 1 0⟩ crystal showing Kikuchi lines when the probe is well overfocused.

dependence on precise instrumental parameters and specimen thickness. Bright intensity peaks correspond to the locality of atomic columns: this is effectively "incoherent imaging" [7].

To form a Z-contrast image, the STEM objective aperture must be inserted to cut out high-angle rays, and an annular detector inserted after the projector lens system. The post specimen lens and detector system for a typical JEM-2010F is shown in Fig. 7. Two detectors are available and the microscope has a Gatan imaging filter (GIF) for energy-filtered imaging and spectroscopy. The upper detector can be centered over the coma-free axis by simply observing the Ronchigram on the microscope phosphor screen. To align the second detector, the GIF CCD camera must be used to observe the shadow image. In this case, there is a disadvantage that the exact inner angle of the detector is not known, because it does not extend all the way up to the lip of the GIF entrance aperture. Variation of the camera length, using the projector lenses, allows the effective inner angle of either detector to be continuously varied. In high-resolution STEM alignment, approximately 12 and 4 cm camera lengths are used for imaging with the upper and lower annular detectors, respectively. These settings ensure the detector inner angles are at least three times the Scherzer convergence angle, and therefore that incoherent imaging dominates.

The use of the electron Ronchigram for alignment allows the introduction of the STEM objective aperture to be postponed until the operator is ready to begin scanning and image acquisition from a well defined and accurately tilted specimen area. This is advantageous since the build up of carbon contamination and onset of beam damage is usually only significant when the aperture is in and the probe intensity is concentrated on a subnanometer scale. On insertion of an aperture, a coherent CBED pattern is formed with the stationary probe. Final adjustments to the specimen tilt can be made and an image acquired by switching on the probe raster. The objective lens focus can also be set with the Ronchigram or CBED pattern, by maximization of the visible lattice fringe widths; only very fine adjustment should then be necessary as the image itself is observed.

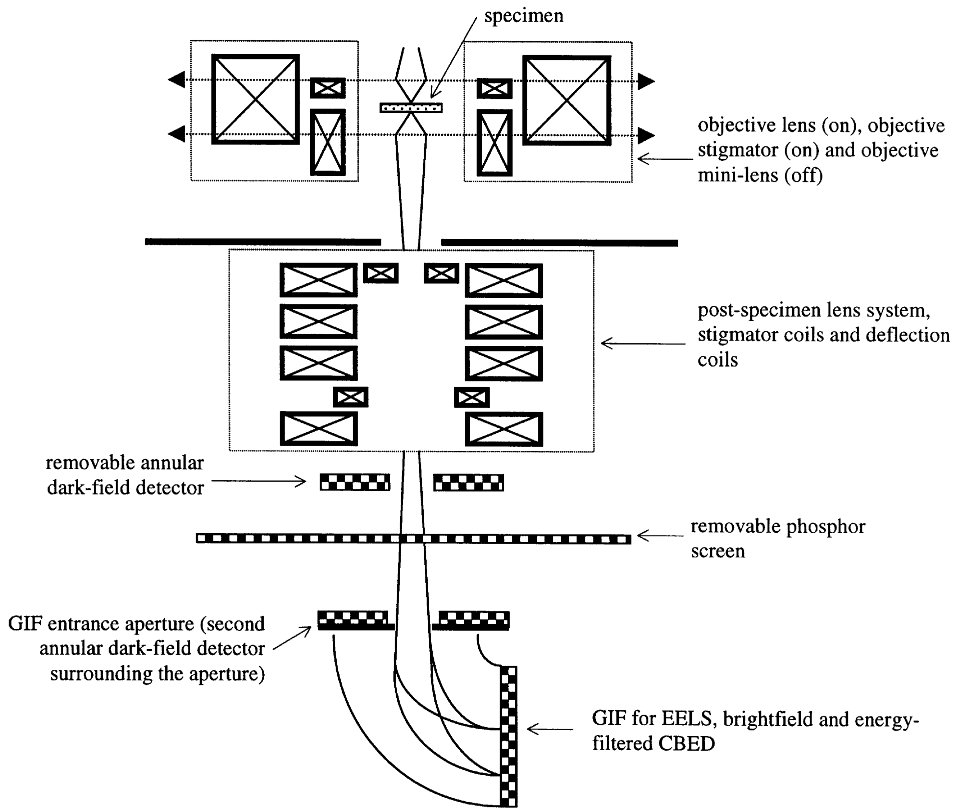


Fig. 7. Schematic diagram of the post-specimen electron optics and detector arrangement in the JEOL JEM-2010F transmission electron microscope.

### *2.4. EELS spectrum acquisition*

EELS spectra can be acquired with the same illumination electron optical settings, and thus the same probe size as for imaging. By collecting electrons over large angles about the optic axis (typically those not intercepted by the annular, Z-contrast detector), diffraction effects are to a significant extent averaged out. EELS spatial resolution is then maximized and is of the order of the probe intensity FWHM at Scherzer focus [15,16] (for an accurate, quantitative resolution definition effective inelastic scattering impact parameters and probe intensity level outside the central peak must also be considered). This arrangement compromises the attainable energy resolution, but often not by enough to degrade EELS fine structure features that are important for analysis of the specimen electronic structure [15,16]. In the JEM-2010F, the second, lower annular dark-field detector is used to position the beam because it surrounds the GIF entrance aperture. By setting the projector lenses to give a short camera length (1–4 cm), the detector inner angle and GIF collection angles are simultaneously set to the desired large values. The probe can be positioned to near-Ångstrom precision with respect to atomic columns shown in the incoherent image from the lower annular detector; spectra are subsequently taken. By acquiring images before and after each EELS spectrum, the presence of specimen drift with respect to the probe can be checked.

## 3. Measurement of the STEM spatial resolution

The method and properties of Z-contrast imaging have been discussed elsewhere [13,14,17–19].

Experimentally, such images are found to be extremely robust to changes in specimen thickness and to slight focus variations: the images are essentially incoherent. Then the image intensity is given directly by convolution of two functions: a point spread component that is the probe intensity distribution, and an object function that approximates well to the square of the specimen potential. Because of this simple convolution form, analysis of the transfer of spatial frequencies to the Z-contrast image can be used to experimentally gain a first estimate of the probe intensity distribution and to compare this to the expected optimum form near Scherzer focus.

Fig. 8a shows a Z-contrast image of Si ⟨1 1 0⟩ at approximately Scherzer focus. On passing through

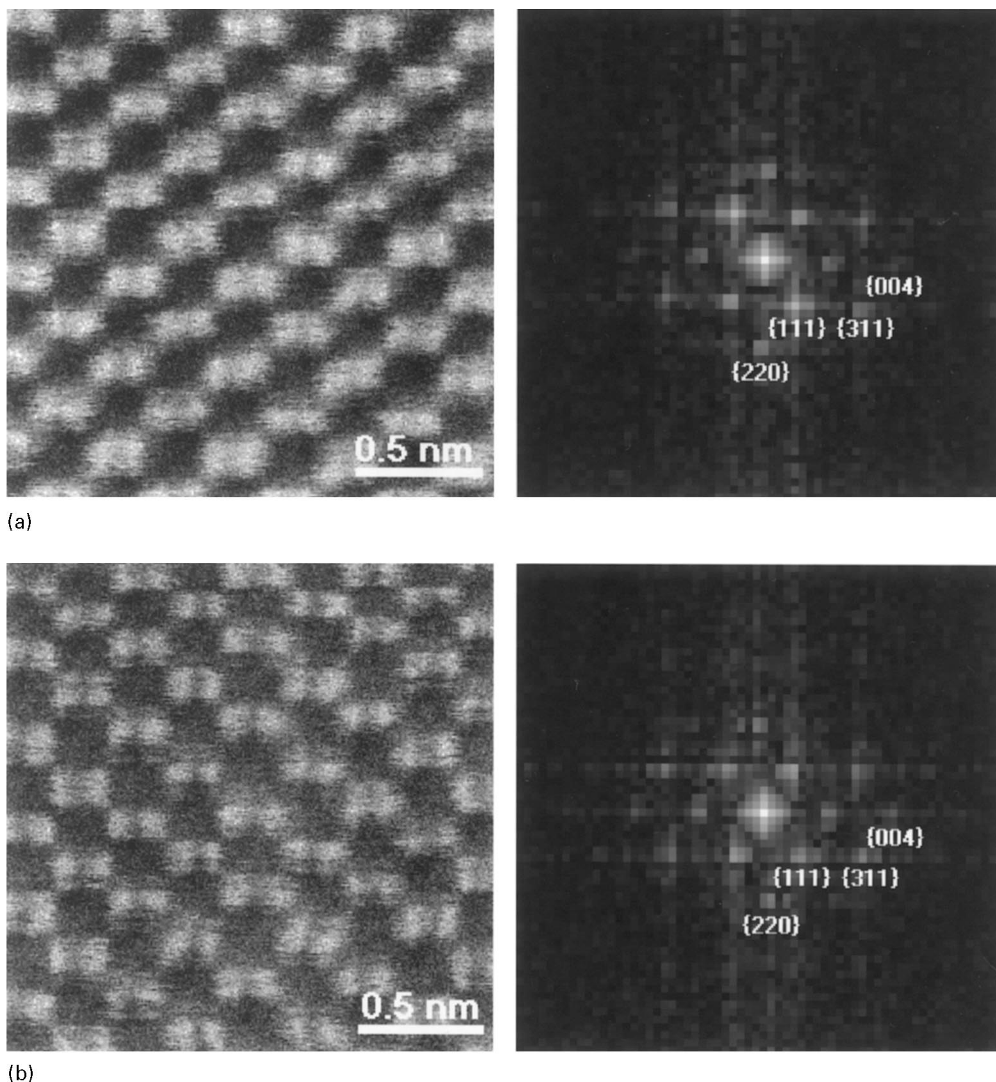


Fig. 8. (a) [left] Z-contrast image of Si ⟨1 1 0⟩ at approximately Scherzer focus. [right] Power spectrum of the Scherzer focus Si ⟨1 1 0⟩ image (logarithmic gray scale). The highest spatial frequencies present are the {0 0 4} reflections which are just visible. (b) [left] Z-contrast image of Si ⟨1 1 0⟩ at an underfocus of approximately 10 nm with respect to the Scherzer condition. [right] Power spectrum of the underfocused Si ⟨1 1 0⟩ image (logarithmic gray scale). The highest spatial frequencies present are the {0 0 4} reflections.

focus, there is no observable contrast reversal effect in the image. Pairs of atom columns are visible as peaks in the intensity: they come in and out of focus without any change of position as the lens excitation is altered. A power spectrum of the image is also shown in Fig. 8a. Information transfer occurs for all reflections up to $\{0\,0\,4\}$; this corresponds to a real space distance of 0.136 nm. The characteristic dumbbell structure of the tetrahedral semiconductor can be discerned. In Fig. 8b the same specimen area was imaged slightly under focus ( $\approx 10$ nm) with respect to Fig. 8a. The dumbbells are more clearly separated at the expense of a relatively increased background signal, visible between the intensity peaks. This suggests that the defocusing has the effect of reducing the width of the probe intensity central maximum (increased resolution), but puts more current into probe "tails" away from the probe center (increased background). Both Fig. 8a and Fig. 8b had 8.5 s acquisition times. It is worthwhile to note that attenuation and eventual truncation of information passed to the image at higher spatial frequencies (smaller real distances) means that the observed dumbbell separations will not be precisely 0.136 nm. However, the effective incoherence of Z-contrast imaging still results in intensity peaks corresponding closely to the atomic column sites at all sensible focus settings.

It is possible to arrive at an estimate of the probe intensity distribution function by performing a deconvolution from the experimental image [20]. If the Z-contrast image is assumed to be perfectly incoherent, the image intensity is given by

$$i(\boldsymbol{r}) = p^2(\boldsymbol{r}) \otimes o(\boldsymbol{r}), \quad (1)$$

where $p^2(\boldsymbol{r})$ is the probe intensity function and $o(\boldsymbol{r})$ is the specimen object function. Using upper case letters for the Fourier transform of the above quantities, the expression for the image power spectrum can be written

$$I(r') = P^2(r') \times O(r') \quad (2)$$

after application of the convolution theorem ($\boldsymbol{r}'$ is the reciprocal-space frequency coordinate and $P^2(\boldsymbol{r}')$ is the transfer function for Z-contrast imaging). Nellist [20] has suggested that the form of the object function can be assumed to consist of Dirac delta functions at atomic column sites, weighted by $Z^2$ (square of the atomic number) of the relevant species in each column. $P^2(\boldsymbol{r}')$ can therefore be estimated at discrete points in reciprocal space, by looking at the magnitude of peaks in the power spectrum. Finally, by performing an inverse Fourier transform, the probe intensity function, $p^2(\boldsymbol{r})$, can be calculated.

Fig. 9a and Fig. 9b show the experimentally determined Z-contrast transfer functions of the JEM-2010F, corresponding to the focus conditions of Fig. 8a and Fig. 8b, respectively. Linear interpolation between each data point in reciprocal space yields the estimated transfer functions. Both are known to decay to negligible values at approximately $(8.0\ \text{nm})^{-1}$, since the $\{331\}$ frequency component cannot be detected in either experimental image. For comparison, the theoretical transfer functions for the optimum Scherzer probe at 200 kV (underfocus of 35.4 nm) and for a probe a further 10.0 nm underfocused are superimposed on the relevant plot. In each case, for the experimentally derived transfer functions, $P^2(0)$ was fitted by constraining the gradient of the first linearly interpolated section to be a good match to the simulated equivalent. Comparison of the experimental and simulated transfer functions at higher frequency was used to check the validity of this low-frequency matching. Also, calculating the experimental probe intensity distributions was a further verification of the assumptions used to set $P^2(0)$. Particularly important was that the first probe minimum must be at a reasonable place with a reasonable value. After iteration, significant confidence could be associated with the low frequency from of the transfer function. In all simulations, a spherical aberration coefficient of 0.5 mm was assumed for the probe-forming system. This value has been confirmed experimentally for the same optical conditions used here [21,22]. In Fig. 10a and Fig. 10b the estimated probe intensity functions are shown, corresponding to the calculated transfer from Fig. 9a and Fig. 9b. Superimposed are the relevant simulated probe shapes.

For both defoci under consideration the experimental STEM probe is estimated to be broader than that expected from simulation but has the same shape. The Scherzer estimated shape (corresponding to Figs. 8a, 9a and 10a) has a FWHM of

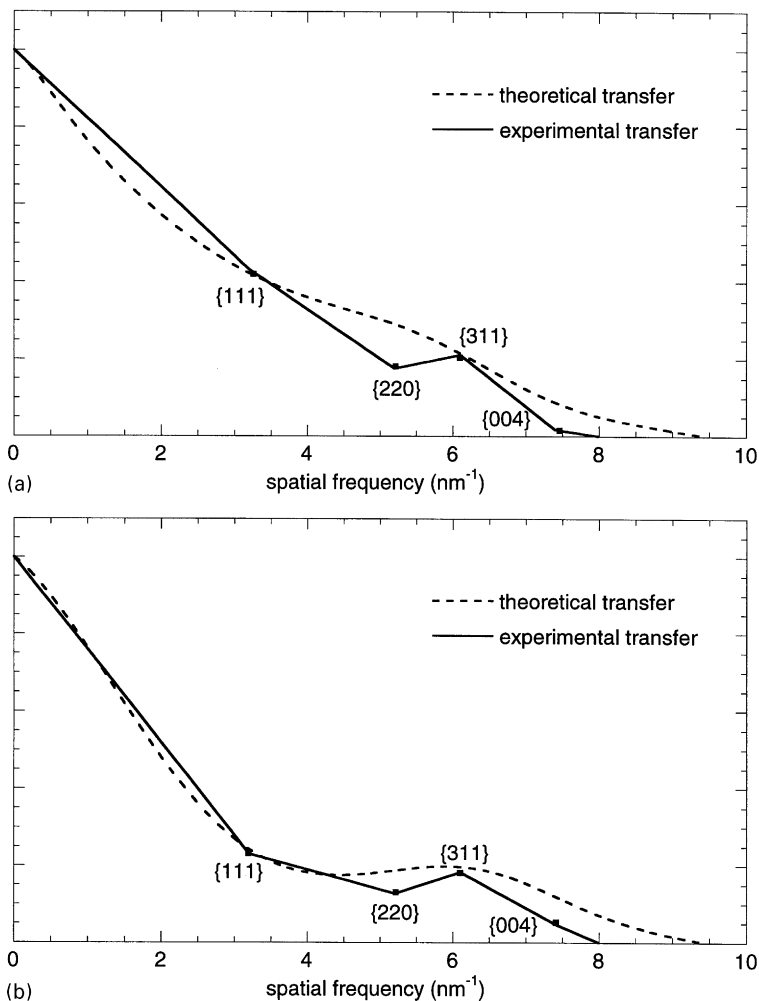


Fig. 9. (a) Comparison of the experimentally determined and theoretical Z-contrast transfer functions for the JEM-2010F – Scherzer focus condition corresponding to Fig. 8a. (b) Comparison of the experimentally determined and theoretical Z-contrast transfer functions for the JEM-2010F – underfocus condition corresponding to Fig. 8b.

0.124 nm: 50% of the probe current is located within a disc of diameter 0.15 nm surrounding the probe center. The further underfocused probe estimation (corresponding to Fig. 8b, 9b and 10b) has a FWHM only slightly less at 0.118 nm. Although, in this crude approximation of the probe shape there is little difference between the two FWHM values, the experimental changes are enough to change the appearance of the dumbbells. Underfocusing by a small amount tailors the transfer function (Fig. 9b) such that higher frequency information (such as the dumbbell separation) is less attenuated. Further defocus would increase this effect but with the undesirable result of significantly reducing transfer of lower frequencies. In terms of the probe shape this means that tails are produced away from the central maximum. Only at the very small defocus settings used in Fig. 8b is this effect not detrimental in terms of introducing intensity peaks away from the atom sites or intolerably reducing the peak to background intensity ratio. Fortunately, the experimental evidence strongly

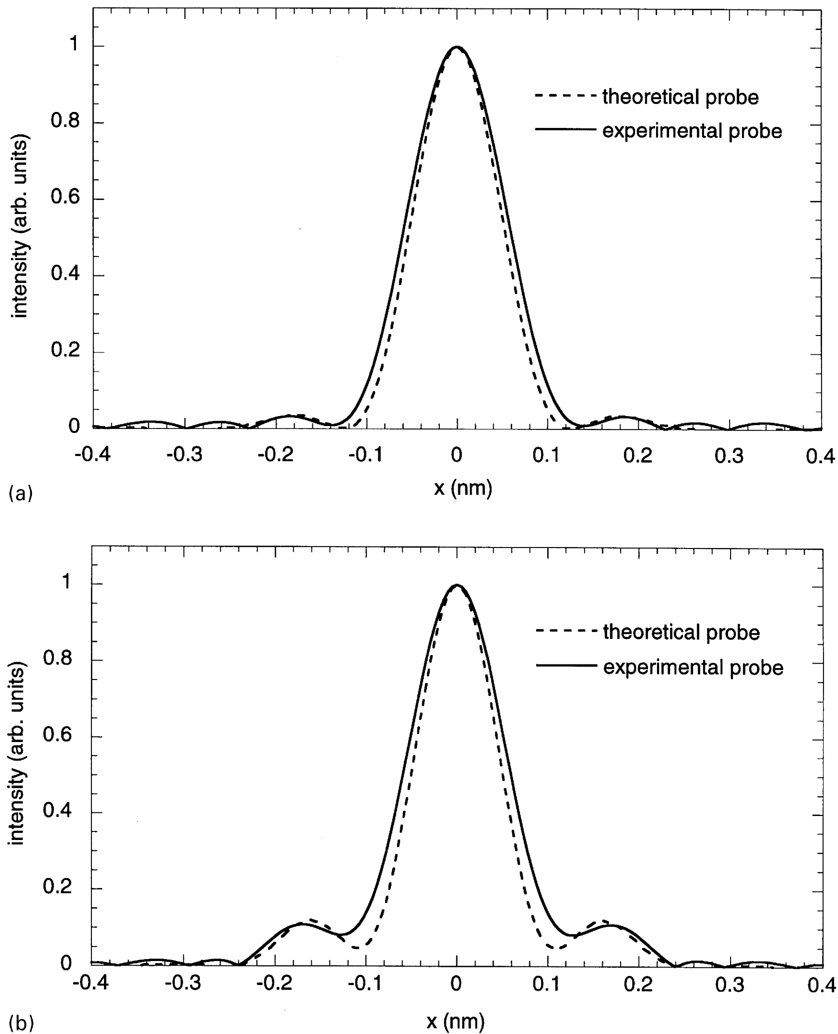


Fig. 10. (a) Comparison of the experimentally determined and theoretical probe intensity distributions for the JEM-2010F – Scherzer focus condition corresponding to Fig. 8a and 9a. The experimental distribution has a FWHM of 0.124 nm. (b) Comparison of the experimentally determined and theoretical probe intensity distributions for the JEM-2010F – underfocus condition corresponding to Fig. 8b and 9b. The experimental distribution has a FWHM of 0.118 nm.

suggests that the Scherzer focus condition is trivial to identify quite accurately with the naked eye, as the focus is adjusted [14]. In practice, the image blurring at other settings is enough to easily avoid use of images that may contain artifacts from the probe tails. The image in Fig. 8a was obtained in this way. Careful observation of the calculated probe intensity first minimum (it does not quite fall to zero) and of the transfer function at high frequency (it rises too abruptly at about $6\,nm^{-1}$) suggest that this image was very slightly underfocused with respect to the Scherzer condition. However, it is much too close to depart radically from the Scherzer probe shape and does not have significant tails that would hamper image interpretation or EELS spatial resolution.

The slightly broader profile of the estimated probe shapes, compared to relevant simulations, may be due to incoherent broadening of the probe due to small, residual mechanical and electrical

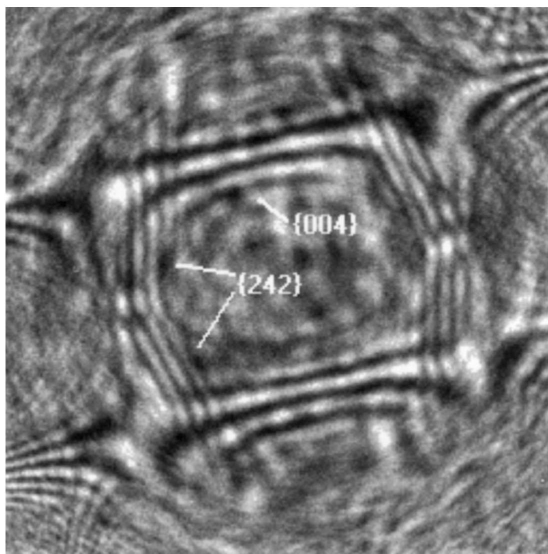


Fig. 11. Ronchigram of Si ⟨2 1 0⟩. Lattice fringes corresponding to the {0 0 4} (0.136 nm) and {2 4 2} (0.111 nm) crystal planes are visible.

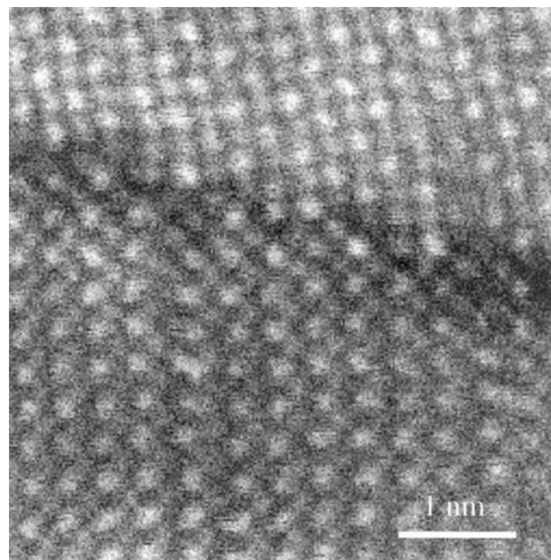


Fig. 12. Z-contrast image of a Σ5 grain boundary in $SrTiO_3$. Acquisition time was 4.3 s.

instabilities, or the effect of finite electron source size. This has been investigated by inspecting the Ronchigram of Si ⟨2 1 0⟩. In this orientation, the lower order diffracted beams correspond to the {0 0 4} planar spacing (0.136 nm) and to the {2 4 2} spacing (0.111 nm). Fig. 11 shows that lattice fringes can be observed that correspond to these spacings. The probe-forming optics were set as for Z-contrast imaging and a 0.5 s exposure onto a slow scan CCD camera was used in acquisition. This indicates that the probe is not incoherently broadened by much more than about 0.1 nm. The {2 4 2}-type fringes are weaker than the {0 0 4}. It is not currently known if smaller spacing lattice fringes can be observed for reasonable probe currents, though this is good evidence suggesting the Scherzer probe size of the JEM-2010F is approaching the minimum value set by the objective lens spherical aberration and the electron energy.

## 4. STEM analysis of a $SrTiO_3$ grain boundary

Using similar optical conditions to the above analysis, the small probe has been used to image a 36.5° Σ5 [0 0 1] tilt grain boundary in a strontium titanate ($SrTiO_3$) bi-crystal. In this condition, the probe current was approximately 15 pA, as measured by a calibrated, conducting phosphor screen. This current is sufficient to acquire images, such as that shown in Fig. 12, with an acquisition time of 4.3 s (mains locked $256 \times 256$ image). Such short acquisition times are advisable since specimen drift will tend to distort the scanned image over long periods of time. Also beam damage to sensitive specimens can be kept to a minimum in this way. Inspection of Fig. 12, and comparison to equivalent atomic resolution images from the 300 kV dedicated STEM [23], shows that the incoherent Z-contrast model holds up well, even in the locality of a grain boundary. With further refinement possible using such methods as maximum entropy reconstruction, atomic column positions can be determined to an accuracy of around 0.02 nm [1]. Additionally, the previously reported $SrTiO_3$ [0 0 1] tilt boundary "structural units" and the $2 \times 1$ column reconstruction contained within them [1], can be identified at this interface.

Experimentally, contrast reversals are not observed in this image, and the strontium columns consistently appear brighter than those of titanium–oxygen due to their higher atomic number.

This is important for the analysis of the grain boundary, where thickness is likely to decrease due to preferential ion milling during specimen preparation. In principle, it should also be possible to directly locate columns where dopants of different atomic number are located using this Z-contrast technique. However, the strain at a grain boundary can be expected to lead at least to some modification to the column intensities [14]. Although there is no observed contrast reversal, the strain can affect the expected atomic number sensitivity in a non-trivially predictable manner. For this reason the images should largely be interpreted qualitatively. In addition, EELS can be acquired from the grain boundary core. At this point, the benefit of the experimental parameters for STEM becomes apparent. The detector geometry enables spectroscopy to be performed at the same time as the imaging process. This means that the Z-contrast image can be used to position the probe with atomic precision to acquire the spectrum [2,3,24]. Provided the experimental conditions are tailored correctly, the same convolution of the probe with an object function that is valid for Z-contrast imaging applies to the spectrum. The EELS spatial resolution can then approach the atomic scale [15,16].

EELS spectra were acquired from the bulk and the grain boundary region of this $SrTiO_3$ specimen. Fig. 13 shows typical spectra, obtained with a stationary probe positioned both over part of the bulk crystal and at the grain boundary. The camera length used was 4 cm, which corresponded to a spectrometer collection angle of around 40 mrad. This high angle was used to suppress the contribution of diffraction effects in much the same way as is done in Z-contrast imaging [15,16]. A nominal dispersion of 0.3 eV/channel was used, and total acquisition time was 12 s.

Also shown in Fig. 13 is a comparison of the JEM-2010F spectra with equivalents obtained from the VG microscopes HB501 cold field emission STEM (in the VG case, the spectra are 10 s acquisitions). At these high collection angles, the energy resolutions are observed to be similar at just under 1 eV. The VG instrument has the advantage of the lower intrinsic emission energy distribution width; however, in this particular case the spectrometer aberrations dominate the spectrum

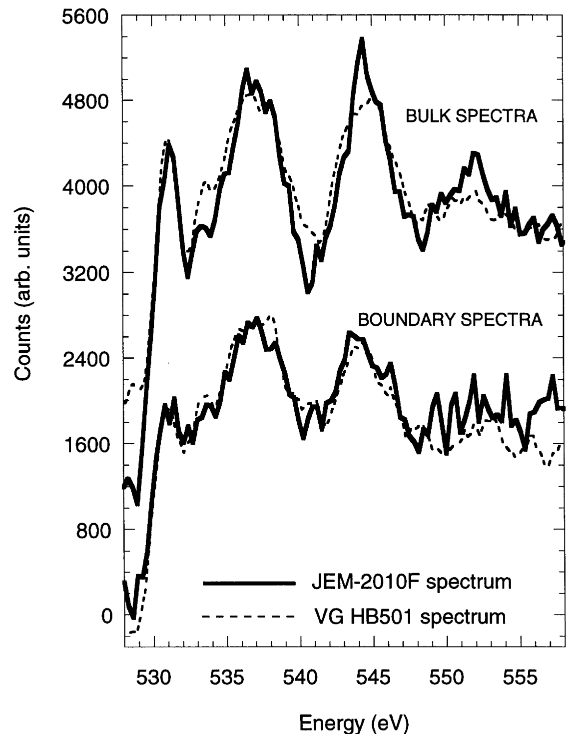


Fig. 13. Comparison between bulk and grain boundary EELS spectra of $SrTiO_3$, using the same probe conditions as for atomic resolution imaging. Also shown (dotted lines) are spectra obtained, using similar probe and spectrometer settings on a cold field emission STEM.

energy resolution. Also, the peak to background ratios are comparable, showing that similar information can be obtained from either microscope. The FWHM of the probe intensity distribution in the dedicated 100 kV STEM is larger, at around 0.22 nm.

It should be noted that this grain boundary was expected to be iron (Fe) doped. However, no trace of Fe segregation was found at the boundary, despite an expected doping concentration (approximately 5%) that should be easily observable by EELS. In fact, the fine structure changes that occur in the oxygen K-edge are similar to those recorded from an undoped boundary [1] using a VG STEM (Fig. 13). This is in marked contrast to the expected fine-structure changes that occur when a significant concentration of dopants is segregated at the grain boundary [24].

## 5. Conclusions

The most successful way of aligning and characterizing a small probe in the electron microscope is by using the electron Ronchigram. Such a shadow image allows fine alignment of specimen tilt and of the illumination optics, in addition to astigmatism correction to a high degree of accuracy. The coma-free axis is trivial to locate from the pattern and it can be used as a reference point for positioning of all the other imaging components, such as apertures and detectors. In this way, it was possible to form a probe in the 200 kV field-emission microscope capable of passing frequencies of $(0.136\,\mathrm{nm})^{-1}$ to a Z-contrast image. Using the power spectrum of the image of a perfect crystal, the probe intensity profile could be estimated and had a FWHM of 0.12 nm. Spherical aberration of this microscope is known to limit the resolution to around this level; therefore, the source size and instability effects do not dominate experimentally: they cause only a minor incoherent broadening of the probe.

The flexibility of the projector lens system allows concurrent Z-contrast imaging and EELS spectrum acquisition without changing the microscope controls. Using a large collection angle, EELS spectra of $SrTiO_3$ were acquired from the bulk crystal and at atomic column sites in a $\Sigma 5$ $36.5^{\circ}$ grain boundary. The probe was positioned by using the intensity peaks of the Z-contrast image. With relatively short acquisition times of a few seconds, high spatial resolution spectra were obtained with energy resolution sufficient to see the core-loss fine structure. A probing of various grain boundary sites revealed no detectable iron dopant segregation at the boundary.

## Acknowledgements

The authors would like to thank Susanne Stemmer for provision of specimens and assistance with the EELS experiment. Yan Xin is also thanked for making her specimens available. This research is funded by the NSF (grant number DMR-9601792) and by the DOE (grant number DE-FG02-96ER45610).

## References

[1] N.D. Browning, S.J. Pennycook, Direct experimental determination of the atomic structure at internal interfaces, J. Phys D 29 (1996) 1779–1798.
[2] N.D Browning, M.F. Chisholm, S.J. Pennycook, Atomic resolution chemical analysis in the scanning transmission electron microscope, Nature 366 (1993) 143–146.
[3] P.E. Batson, Simultaneous STEM and electron energy loss spectroscopy with atomic column sensitivity, Nature 366 (1993) 727–729.
[4] J.M. Cowley, Electron diffraction phenomena observed with a high resolution STEM instrument, J. Electron. Microsc. Tech. 3 (1986) 25–44.
[5] J.M. Cowley, Image contrast in transmission scanning electron microscopy, Appl. Phys. Lett. 15 (1969) 58–60.
[6] E.M. James, Ph.D. Thesis, University of Cambridge, Cambridge, 1997.
[7] S.J. Pennycook, D.E. Jesson, A.J. McGibbon, P.D. Nellist, High angle dark field STEM for advanced materials, J. Electron Microsc. 45 (1997) 36–43.
[8] P.D. Nellist, Y. Xin, S.J. Pennycook, Direct structure determination by atomic resolution incoherent STEM imaging, Inst. Phys. Conf. Ser. 153 (1997) 109–112.
[9] P.D. Nellist, B.C. McCallum, J.M. Rodenburg, Resolution beyond the information limit in transmission electron microscopy, Nature 374 (1995) 630–632.
[10] O.L. Krivanek, N. Dellby, A.J. Spence, L.M. Brown, Spherical aberration correction in dedicated STEM, in: H.A.C. Benavides (Ed.), Electron Microscopy 1988, Proceedings of ICEM14, vol. 1, IoP, Bristol, 1998.
[11] J.A. Lin, J.M. Cowley, Calibration of the operating parameters for an HB5 STEM instrument, Ultramicroscopy 19 (1986) 31–42.
[12] O. Scherzer, Über einige Fehler von Electronenlinsen, Zeit. Phys. 101 (1936) 593–603.
[13] D.E. Jesson, S.J. Pennycook, Incoherent imaging of thin specimens using coherently scattered electrons, Proc. Roy. Soc. London A 441 (1993) 261–281.
[14] D.E. Jesson, S.J. Pennycook, Incoherent imaging of crystals using thermally scattered electrons, Proc. Roy. Soc. London A 449 (1995) 273–293.
[15] N.D. Browning, S.J. Pennycook, Atomic resolution electron energy loss spectroscopy in the scanning transmission electron microscope, J. Microscopy 180 (1995) 230–237.
[16] S.J. Pennycook, D.E. Jesson, N.D. Browning, Atomic-resolution electron energy loss spectroscopy in crystalline solids, Nucl. Instr. and Meth. 96 (1995) 575–582.
[17] P. Hartel, H. Rose, C. Dinge, Conditions and reasons for incoherent imaging in STEM, Ultramicroscopy 63 (1996) 93–114.
[18] A. Amali, P. Rez, Theory of lattice resolution in high angle annular dark-field images, Microsc. Microanal. 3 (1997) 28–46.
[19] S. Hillyard, R.F. Loane, J. Silcox, Annular dark-field imaging: resolution and thickness effects, Ultramicroscopy 49 (1993) 14–25.

[20] P.D. Nellist, S.J. Pennycook, Accurate structure determination from image reconstruction in ADF STEM, J. Micros. 190 (1998) 159–170.

[21] E.M. James, N.D. Browning, A.W. Nicholls, M. Kawasaki, Y. Xin, S. Stemmer, Quantifying the STEM performance of the JEOL JEM-2010F, JEOL News 33 (1998) 9–14.

[22] E.M. James, N.D. Browning, A.W. Nicholls, M. Kawasaki, Y. Xin, S. Stemmer, Demonstration of atomic resolution Z-contrast imaging by a JEOL JEM-2010F scanning transmission electron microscope, J. Electron Microsc. 47 (1998) 561–574.

[23] M.M. McGibbon, N.D. Browning, A.J. McGibbon, M.F. Chisholm, S.J. Pennycook, Atomic structures of asymmetric [0 0 1] tilt boundaries in $SrTiO_3$, Philos. Mag. A 73 (1996) 625–641.

[24] G. Duscher, N.D. Browning, S.J. Pennycook, Atomic column resolved EELS, Phys. Stat. Sol. 166 (1998) 327–342.